TECHNICAL ARTICLE

Dual-Wire Plasma Arc Additively Manufactured SS 316L-Inconel 625 Functionally Graded Material: Microstructure Evolution and Mechanical Properties

Xiaoyan Yu, Jiaxiang Xue, Qingkai Shen, Zehong Zheng, Ning Ou, and Wei Wu

Functionally graded material (FGM) is an appropriate response to high-performance and multi-functional applications. In this research, dual-wire plasma arc welding can be used to fabricate SS 316L-Inconel 625 FGM with a composition gradient of 50 wt.% by adjusting the volume fraction of welding wire delivered to the melt pool. The phase evolution, microstructure, composition, microhardness and tensile properties of different composition regions along the building direction were analyzed. The results show that good bonding in the bi-metallic interface region and defect-free microstructure. The microstructure along the deposition direction is mainly columnar and equiaxed dendritic structure, and the grain growth direction is mainly along the deposition direction. The existence of Laves phases is proved by EDS mapping and point detection. Due to remelting, an error is existed between the actual composition distribution and the designed discrete gradient. The microhardness value decreases first, and reaching a minimum at the bi-metallic interface of the 100–50 wt.% SS 316L, and then increase gradually (157 HV-208 HV). The ultimate tensile strength, yield strength and elongation are 554.12 ± 7.44 MPa, 340.79 ± 4.13 MPa and 26.65 ± 0.27%, respectively. From the feasibility study, the dual-wire plasma arc welding provides a novel additive manufacturing process for the FGMs.

1. Introduction

The nickel-based superalloys and stainless steels have good corrosion properties at high temperatures. Besides, nickel-based superalloys have better strength, and stainless steels has lower cost and weight (Ref 1, 2). These characteristics make two alloys widely used in aerospace, chemical, petrochemical, marine and other high-temperature and corrosion industries (Ref 3). However, with the continuous development of these industrial fields, components are required to be able to operate simultaneously under high temperature, high pressure, high-speed rotation and extreme load (Ref 4, 5), which requires parts have different mechanical properties in different directions. Based on this typical application, the mechanical properties of one alloy (Inconel 625 or SS 316L) are not sufficient. Therefore, some researchers proposed to use the stainless steel/nickel-based FGMs (Ref 6). In stainless steel/nickel-based FGMs, the composition or micro (macro) structure changes gradually along one or more directions, so that the microstructure and mechanical properties can change accordingly (Ref 7, 8, 9). Stainless steel/nickel-based FGMs that have been successfully manufactured include SS 304L-Inconel 625 (Ref 10), SS 316L-Inconel 718 (Ref 11), SS 316L-Inconel 625 (Ref 6) and SS 321-Inconel 625 (Ref 12) etc.

The emergence of additive manufacture (AM) opened a new chapter for metal-FGM (Ref 13). The preparation of FGM by AM process can alleviate the thermal and residual stresses caused by the difference of thermal expansion coefficient (CTE) at the bi-metallic interface, thereby solving the problem of interface cracking (Ref 14). AM is a very suitable method for manufacturing FGM, and the preparation of metal-FGM by AM process can greatly promote the development of FGMs (Ref 15, 16, 17). AM is divided into two categories based on raw materials: powder and wire (Ref 18), and previous work in the fabrication of stainless steel/nickel-based FGMs by AM process has focused on metal powders (Ref 19, 20). For instance, Su et al. (Ref 21) fabricated SS 316L-Inconel 718 FGMs with different composition gradients (5, 10 and 20 wt.%) by laser metal deposition (LMD). Savitha et al. (Ref 6) manufactured discrete and compositionally graded SS 316-Inconel 625 FGMs by the Laser Engineered Net Shaping (LENS). Carroll et al. (Ref 10) fabricated the SS 304L-Inconel 625 FGM by directed energy deposition (DED) technology.

Compared with laser metal deposition (LMD), wire and arc additive manufacturing (WAAM) has the advantages of high raw material utilization, high deposition rate, low equipment cost and large-size part, which has attracted extensive research attention (Ref 22, 23, 24). In WAAM process, the mixing ratio and deposition thickness can be

Xiaoyan Yu, Jiaxiang Xue, Qingkai Shen, Zehong Zheng, and **Ning Ou**, School of Mechanical and Automotive Engineering, South China University of Technology, Guangzhou 510641, China; and **Wei Wu**, School of Electrical and Mechanical, Guangdong Polytechnic Normal University, Guangzhou 510641, China. Contact e-mail: mejiaxue@scut.edu.cn.

controlled accurately by adjusting the wire feeding speed of two welding wires with different composition, and the fabrication of FGM by WAAM has become a promising solution (Ref 25, 26). Thus, many researchers used the WAAM process to fabricated FGMs such as AISI 410-AWS ER70S-6 (Ref 22)), TC4-SS 316L (Ref 27), W-Mo (Ref 28), CoCrFeNi(SiC)x (Ref 25), Fe-FeAl (Ref 29), Ti₆Al₄V-Inconel 625 (Ref 30), steel-copper (Ref 31) and Fe₃Ni-FeNi (Ref 32) et al. Similarly, the WAAM technology can also be used to manufacture bi-metallic structures composed of Inconel superalloy and stainless steel (Ref 10). Senthil et al. (Ref 33) proved that it was feasible to deposited nickel-based superalloys directly on stainless steel by Cold Metal Transfer (CMT) technology, and the Fe and Ni elements changed significantly at the interface. No defects were found at the interface, and Inconel 825 and SS 316L combined well, but the mechanical properties at the interface changed suddenly, and the hardness and tensile strength were lower than SS 316L and Inconel 825. Kumar et al. (Ref 12) manufactured two Inconel 625-SS 304L bi-metallic structures without and with intermediate layer by double wire metal inert gas (MIG) welding. And the results showed that the composition of the Inconel 625-SS 304L bi-metallic structure with intermediate layer changed gradually, and the mechanical properties were more excellent. Zhang et al. (Ref 34) fabricated Inconel 625/HSLA-steel FGM by the WAAM process, and electromagnetic stirring (EMS) technology was used to improve the composition dilution rate, refine grains and reduce the precipitation of Laves phase. The results showed that the EMS auxiliary process was helpful to improve the performance of FGM. Therefore, the manufacture of nickel-based/stainless steel FGM by WAAM technology with high efficiency and low cost is the future development trend. Among then, s a kind of WAAM process energy, plasma has been widely used in modification of alloys and the preparation of coatings and FGMs (Ref 35, 36).

In this work, a novel AM process based on dual-wire plasma arc additive manufacturing was proposed for the fabrication of defect-free and reasonable composition distribution of SS 316L-Inconel 625 FGM. The microstructure, composition distribution and mechanical properties of SS 316L-Inconel 625 along the building direction were analyzed. According to the feasibility study, the dual-wire plasma arc welding process can be used to manufacture SS 316L-Inconel 625 FGM, and provides a novel manufacturing process for the nickel-based/stainless steel FGM.

2. Material and Methods

2.1 Wire and Arc Additive Manufacturing Setup

The FGM components from SS 316L to Inconel 625 was deposited by a dual-wire plasma arc welding system, which was composed of a welding power supply (Transmig 550i), two multifunctional automatic argon arc wire feeders (ET-2016), an argon gas (99.99% purity) shielding system, a six-axis welding robot (Fanuc) and a robot controller is shown in Fig. 1(a). SS 316L and Inconel 625 welding wires with a diameter of 1.2 mm were selected to deposited on the surface of a 304L substrate with a dimension of 150 mm × 80 mm × 10 mm. The composition of SS 316L and Inconel 625 wire is shown in Table 1.

In order to ensure well cladding, high current deposition was adopted at the bottom of the SS 316L-Inconel 625 FGM, and the travel speed was 5 mm.s⁻¹. Argon gas (99.99% purity) with a constant rate of 15L/min was selected as shield gas. The length of the thin-wall structure was 125 mm, and the height of welding torch was designed according to the actual layer height to ensure the height was within a fixed range (8-10 mm). The temperature between the layers was measured by a thermocouple, and when the temperature cooled to 200 °C, the next layer was deposited. By changed the wire feed speed of SS 316L and Inconel 625 wires, the transition from SS 316L to Inconel 625 was achieved and the composition gradient was 50 wt.%. The "Zigzag strategy" was adopted for the welding torch trajectory of each layer, and the "cyclic reciprocating" mode was adopted between layers.

2.2 Material Characterization Techniques

Figure 1(b) shows the macrography of SS 316L-Inconel 625 FGM, and the boundaries between layers were clear. The analysis samples of SS 316L-Inconel 625 FGM were sampled by wire-cut electrical discharge machine and the position of analysis samples are shown in Fig. 1(c). Furthermore, the cross-section surface of SS 316L-Inconel 625 FGM was ground from 800 to 7000 grit, and then, polishing with diamond suspension from 2.5 μm and 0.25 μm. The as-polished SS 316L-Inconel 625 FGM were etched for a few seconds to reveal the dendritic microstructures. The X-ray diffraction (XRD) patterns of SS 316L-Inconel 625 FGM was collected using a Rigaku Smartlab D/max/2600PC, and the scanning rate and diffraction angle were set as 4°/min, 20–100°. The microstructure was observed by an optical microscope (OM, ZEISS Vert.A1). The composition along the building direction of 326L-Inconel 625 FGM were analyzed by an energy dispersive spectroscopy (EDS) on the SEM. And the electron backscatter diffraction (EBSD) experiment of cross-section samples of SS 316L-Inconel 625 FGM was conducted using a NOVA 430 field emission scanning electron microscope to investigated the dendrite orientation and grain size in the building direction of SS 316L-Inconel 625 FGM. The microhardness values along the depositing direction were measured using a hardness tester (MVS-1000D1) under a 200 g load and kept for 15 s. The tensile tests were conducted at room temperature by electronic universal tensile machine (CMT5105), with a loading rate of 1.0 mm/min.

3. Results and Discussions

3.1 Evaluation of Microstructure

Figure 2(a) shows the XRD patterns taken form the different composition regions of SS 316L-Inconel 625 FGM (100 wt.% SS 316L, transition zone and 100 wt.% Inconel 625). In agreement with earlier research, the diffraction peaks in the 100 wt.% SS 316L region are consistent of FCC phase (austenite) and a small amount of BCC phase (ferrite), and only the FCC phase is existed in Inconel 625 (Ref 37, 38, 39). The XRD patterns of the transition zone (50 wt.% SS 316L/50 wt.% Inconel 625) is roughly the same as 100 wt.% Inconel 625, and shows a little significant 2 θ change. Therefore, it can prove that the transition zone is also FCC structure (Ref 40). The above phase evolution is due to the formation of a unique austenite
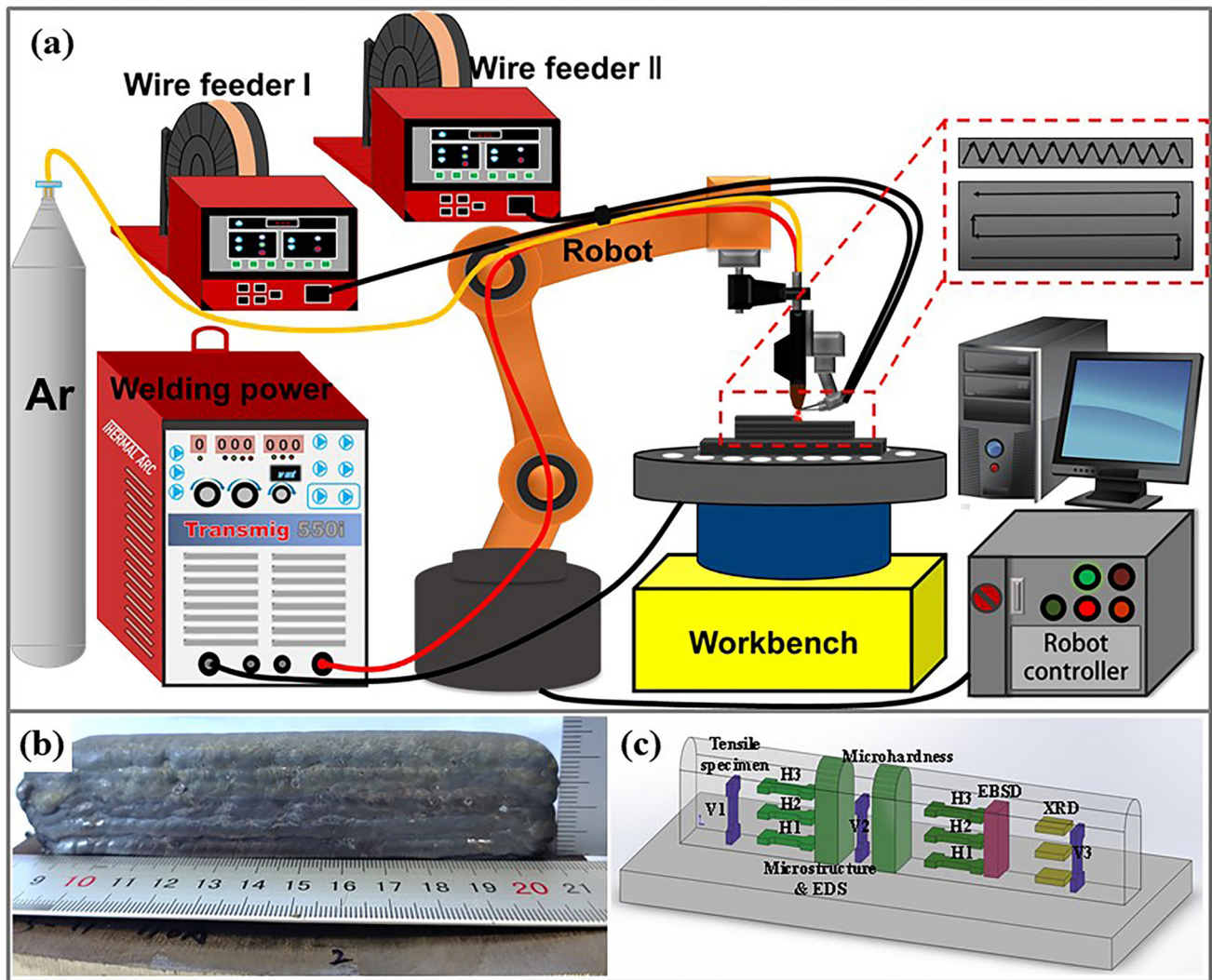
Fig. 1 (a) The WAAM system, (b) A photographic image of the FGM and (c) The sampling position

Table 1 Element of welding wires used in weight percent, wt.%

Element	Cr	Ni	Mn	Si	C	Mo	Ti	Nb	Fe	Al	Co
SS 316L	17	13.5	1	0.5	0.0	2.5	…	…	65.5	…	…
Inconel 625	21	65.7	0.4	0.4	0.0	8.7	0.1	3.4	0.0	0.0	0.3

solidification structure with the increase in Ni element, and the phase of SS 316L-Inconel 625 FGM gradually changes from ferrite/austenite phase to the austenite phase (Ref 41) (see Fig. 2(b)). At the same time, the XRD patterns also demonstrate that the peak height in the γ(200) plane of all SS 316L-Inconel 625 FGM regions is significantly higher than other planes. Previous research indicated that the (200) plane relatively high peak is represented the highly textured columnar dendrites (Ref 40). The peak height of the γ(111) plane in the SS 316L regions is higher than the region of the Inconel 625 and the peak height of the γ(200) plane for SS 316L is lower than Inconel 625. Thus, the results demonstrate that the regions of Inconel 625 have more columnar dendrites and fewer equiaxial dendrites, and the columnar dendrites of crystalline

structure are more uniformly aligned and results in the microhardness value increased (Ref 42). In addition, no other peaks are observed in XRD patterns, so the existence of leaves or other precipitated phases could not be proved. However, this does not rule out the existence of the second phases. It may be that the number of precipitated phases is small or the size is too small to be detected by XRD, so other test methods are needed for further testing.

From the overall cross-section of the deposition parts, the SS 316L-Inconel 625 FGM has good bonding of multi-layered walls and without defects such as cracks and pores, as shown in Fig. 3(a). Normally, the solidification morphology is highly related to the ratio of the temperature gradient (G) and the crystal growth rate (R), and the G/R ratio determines the size of
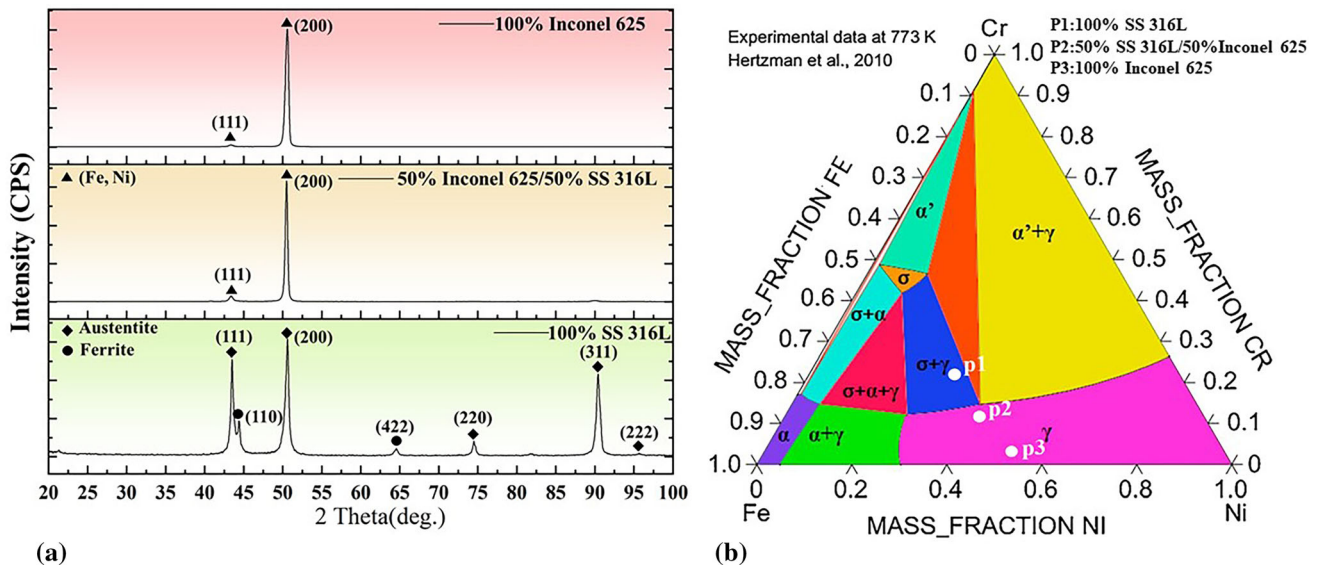
Fig. 2 (a) XRD patterns along the deposited direction and (b) Fe–Cr-Ni ternary phase diagram (773 K) (Ref 39) and three composition regions
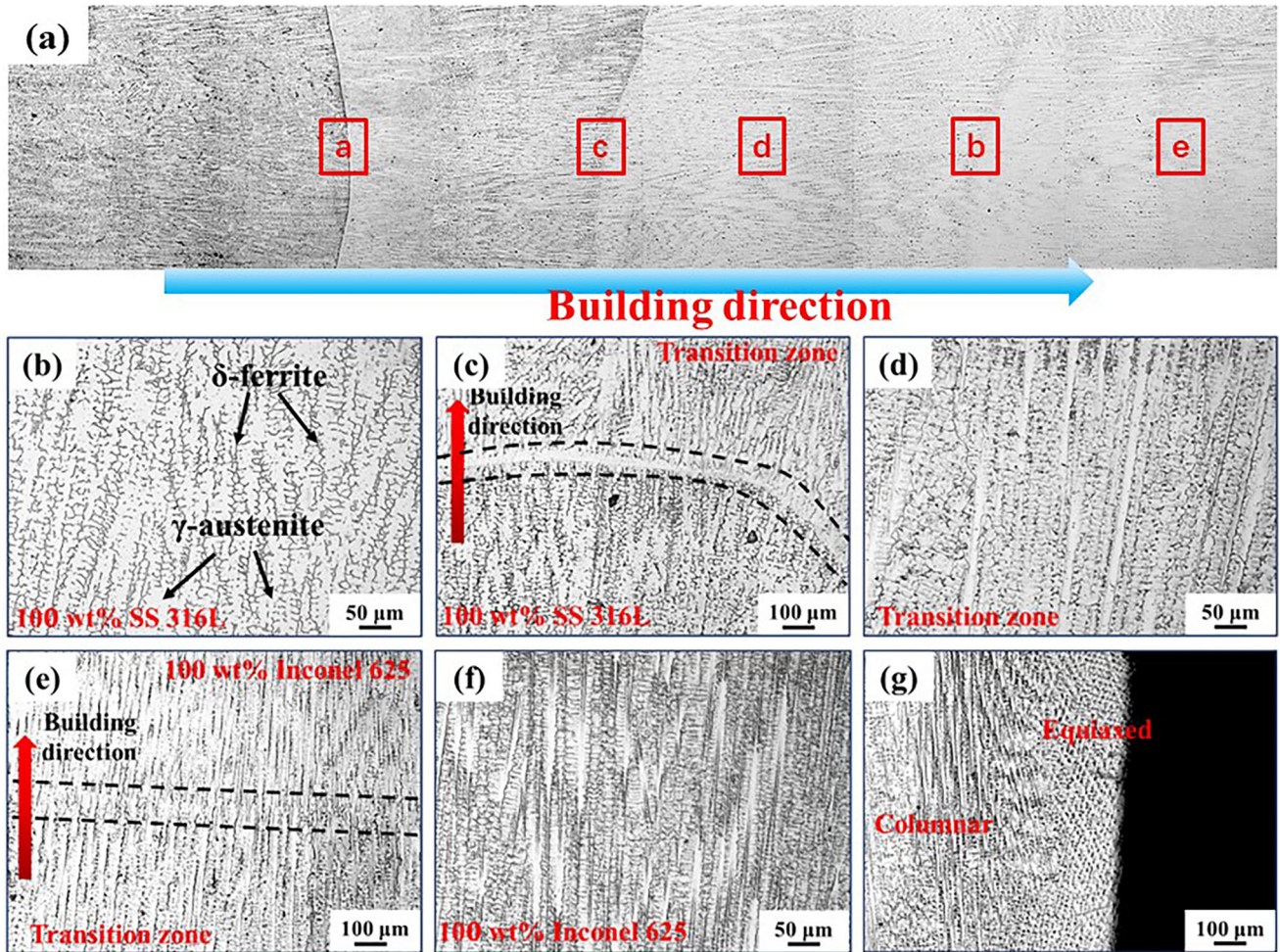

Fig. 3 Microstructure of SS 316L-Inconel 625 FGM gradient cross-section: (a) overall structure, (b) SS 316L side, (c) Bi-metallic interface of 100–50 wt.% SS 316L, (d) 50 wt.% SS 316L, (e) Bi-metallic interface of 50–100 wt.% Inconel 625, (f) Inconel 625 side and (g) The edge areas of FGM

grains structure (Ref 43). The dual-wire plasma arc additive manufacturing process has large heat input and complex thermal cycle, so the G/R ratio is low, and resulting in the formation of columnar or equiaxed dendritic structure (Ref 43). The microstructure of the cross-section of SS 316L-Inconel 625 FGM along the deposition direction is observed by an OM (see from Fig. 3). Due to the high cooling rate during welding process and the substrate acts as a heat sink, directional solidification can be observed in the different composition regions, and there is a strong directional growth in the building direction, which is consistent with the results of XRD patterns (Ref 44). In the 100 wt.% SS 316L region(Fig. 3(b)), the microstructure is characterized by columnar dendrites, which is composed of γ-austenite (FCC, the bright regions) phase and δ-ferrite (BCC, the grey regions) phase (Ref 45), and Carroll et al. (Ref 10) also found the similar situation. Figure 3(c) shows the microstructure of the interface between the 100 wt.% SS 316L and the transition zone (50 wt.% SS316L/50 wt.% Inconel 625). It is observed that the interface with different composition is clear and the micromorphology is changed obviously. The microstructures in the transition zone (see from Fig. 3(d)) are also columnar dendritic structure, but no δ-ferrite is observed (Ref 46, 47). Figure 3(e) shows the micromorphology of the interface between the transition zone (50 wt.% SS 316L/50 wt.% Inconel 625) and 100 wt.% Inconel 625, and the columnar dendrites continue to grow in the interface of different composition (Ref 48). When the content of Inconel 625 increased to 100 wt.% (see Fig. 3(f)), the microstructure is columnar dendritic structure and the primary dendrite arm spacing increased along the building direction (Ref 21). The temperature increases constantly with the number of deposited layers increases due to the AM technology is a serious heat accumulation process. The temperature gradient of the latter deposition layer is lower than that of the previous deposition, so the primary dendrite arm spacing increases (Ref 44, 49). In addition, columnar to equiaxed transition is observed at the edge and top regions of the FGM cross–section (Fig. 3(g)),

which can be attributed to a small amount of heat flowing to the air by thermal radiation (Ref 11).

The high magnification SEM morphology of the microstructure of SS 316L-Inconel 625 FGM is shown in Fig. 4. The δ-ferrite and γ-austenite phases exist in the 100 wt.% SS 316L regions (Fig. 4(a)), the content of Cr and Mo in δ-ferrite phase is more than that in γ-austenite, and the content of Ni is less (Ref 50). And Fig. 4(b) and (c) shows the EDS mapping of transition zone and 100 wt.% Inconel 625, the white second phase can be observed in the inter dendritic regions. Obvious segregation of Mo and Nb elements, it is can be demonstrated the formation of Laves phase. And the existence of brittle Laves phases would soften the matrix by segregation the Nb and Mo elements, and results in the mechanical properties of the SS 316L-Inconel 625 FGM to decrease (Ref 51). Table 2 shows the EDS point detection results of second phase particles in 100 wt.% Inconel 625, with a significant increase in Mo and Nb elements. It is further proved that the Laves phase exists during the WAAM process. The similar results were also found in the study of cladding SS 316L-Inconel 625 FGM superalloy by Chen et al. (Ref 52).

In order to further study the texture of the FGMs, the EBSD analysis is employed in this work. The EBSD micrographs of the SS 316L-Inconel 625 FGM along the building direction are observed in Fig. 5. The color variation in the inverse pole figure (IPF) corresponds to the crystal structure of austenitic grains. The EBSD examination results show that the bi-metallic interface of SS 316L-Inconel 625 FGM along the depositing direction is presented in Fig. 5(a), the microstructure of different composition is mainly FCC and the micromorphology is dendritic. And the grains grow continuously at the SS 316L/ Inconel 625 bi-metallic interface and large elongated columnar dendrites are observed. As demonstrated by Chen et al. (Ref 52), previous grains become nucleation point for the solidification of the subsequent layers due to partial re-melting of the previously deposited layers. The grain size and orientation of SS 316L at the bottom of FGM are shown in Fig. 5(b), and the distribution of grain distribution indicates that the existence of
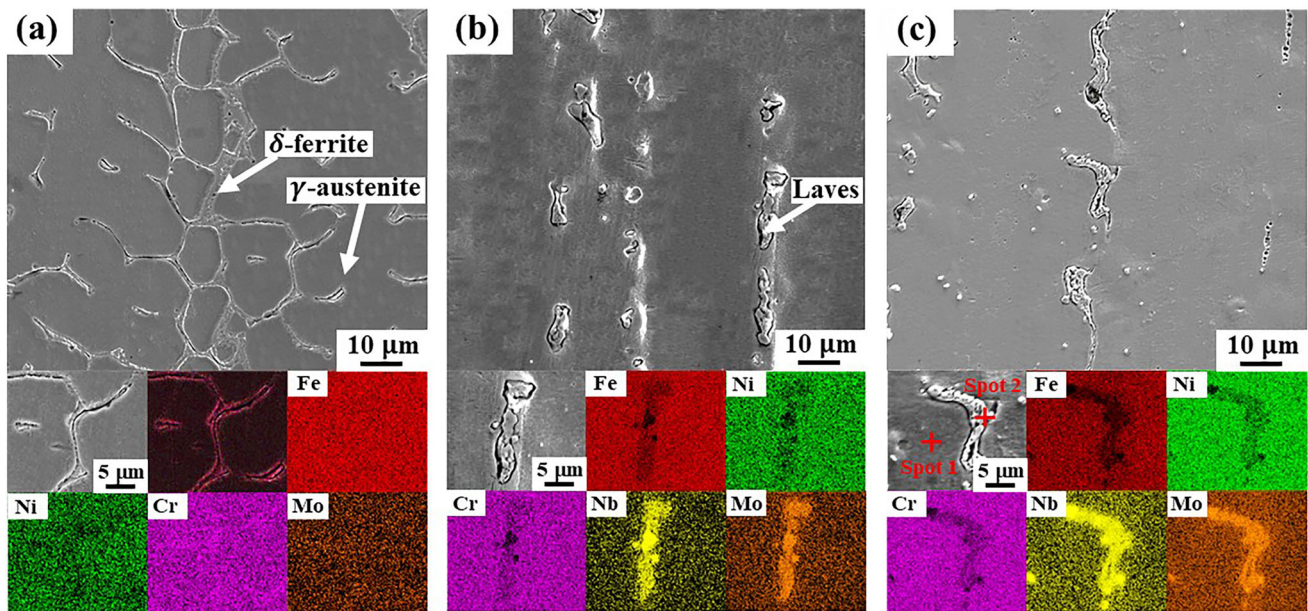
Fig. 4 Microstructure and EDS maps of: (a) 100 wt.% SS 316L, (b) 50 wt.% SS 316L/50 wt.% Inconel 625 and (c) 100 wt.% Inconel 625

Table 2 The EDS point detection results of second phase particles in 100 wt.% Inconel 625

Element	Cr	Ni	Mn	Si	C	Mo	Ti	Nb	Fe	Al	Co
Spot 1	25	70	1	0	0	1	0	1	2	…	…
Spot 2	14	30	…	0	0	9	2	44	1	…	…
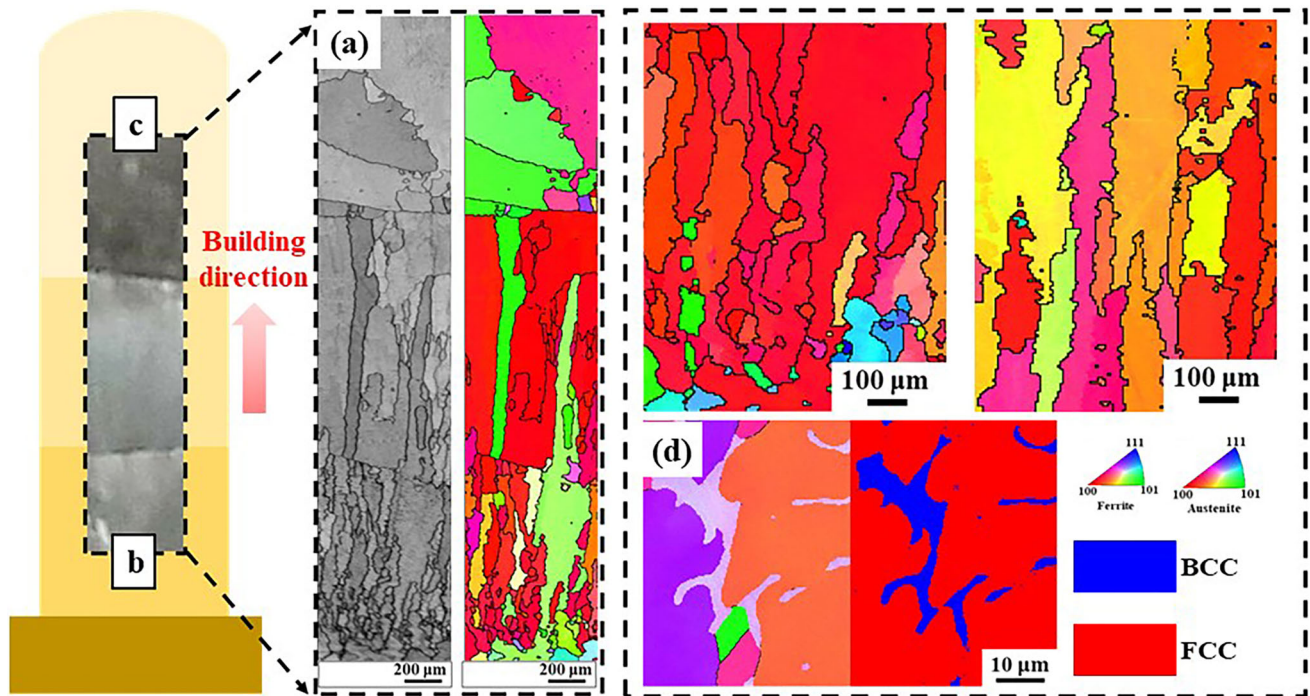
Fig. 5 The EBSD examination results along the building direction: (a) overall structure, (b) SS 316L side and (c) Inconel 625 side

equiaxed and columnar dendrites. Equiaxed dendrites are mainly present at the bottom of SS 316L side, and a transition from equiaxed to columnar dendrites can be observed with the increase in deposition height (Ref 40). The preferred grain growth orientation on the SS 316L side is the < 001 > (red), but the grain orientations on the bottom of SS 316L side also are also < 101 > and < 111 > (green and blue) (Ref 53). In addition, the phase map and IPF map of high magnification morphology in the SS 316L region show that SS 316L region is composed of FCC and BCC phase, and ferrite is distributed within grains and grain boundaries, and exhibit fine vermicular morphology, previous research also found the similar situation (see Fig. 5(d)) (Ref 54). The IPF map highlights that the preferred grain growth of the Inconel 625 region is the < 001 > orientation (red) and the microstructure is predominantly austenitic (see Fig. 5(c)). The second phase are not detected by EBSD results in the 100 wt.% Inconel 625 region (Ref 12). And the grains growth direction of columnar dendrites depends on the heat flow direction and the preferred growth direction during the solidification of Inconel 625, and the microstructure is mainly coarse columnar dendrites and small grains (Ref 53).

3.2 Composition

In order to research the effect of SS 316L/Inconel 625 FGM gradient design on the composition distribution, the semi-quantitative EDS results along the depositing direction are compared with the design composition of the gradient, as shown in Fig. 6. Due to the large heat input and complex thermal cycle in the WAAM process, the deposited metal layer is remelted (Ref 15). Therefore, the actual composition gradient of SS 316L-Inconel 625 FGM has three composition gradients in the transition zone, while the designed composition gradient is only 50 wt.% SS 316L/50 wt.% Inconel 625. The results show that with the addition of Inconel 625, the Fe element decreases significantly and the Ni element increases markedly. Since the content of Cr element in SS 316L and Inconel 625 is not much different, the Cr element in 100 wt.% Inconel 625 region increases slightly. With the continuous addition of Inconel 625, the elements Mo and Nb contained in Laves phase also increased (Ref 21).

3.3 Microhardness

Figure 7(a) shows the microhardness variation of SS 316L-Inconel 625 FGM along the building direction. At the bottom of FGM, the microhardness of the 100 wt.% SS 316L region is firstly decreased due to heat accumulation. And then, the concentration of Inconel 625 in the first transition region is less than 50 wt.% due to the effect of remelting. Therefore, when a small amounts of Inconel 625 (< 50 wt.%) is added and the formation of ferrite is suppressed, a microstructure transformation from primary ferrite to austenite phase is realized (Ref 41),
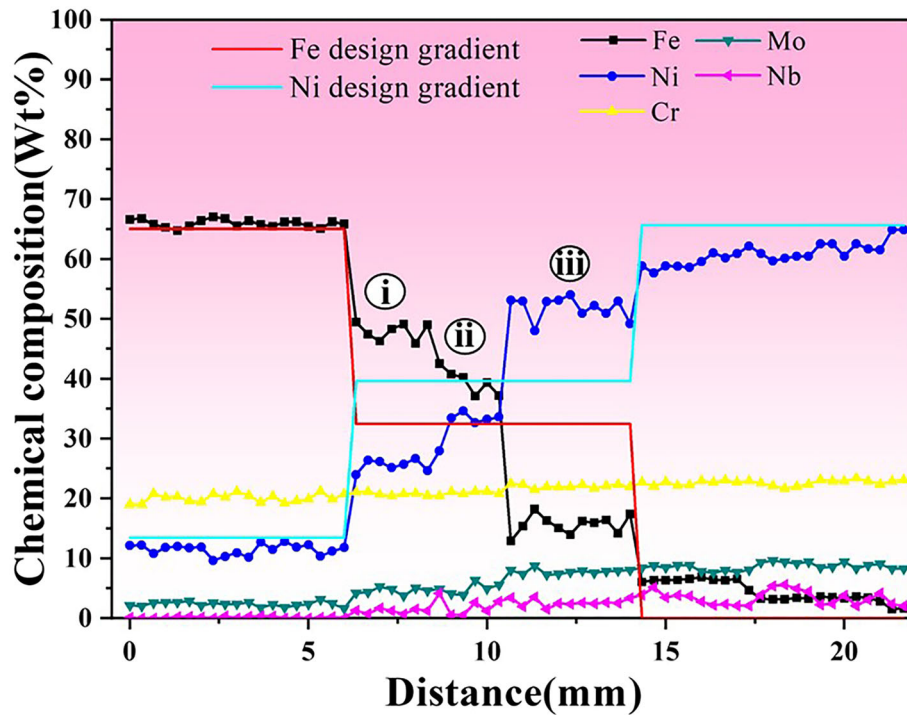
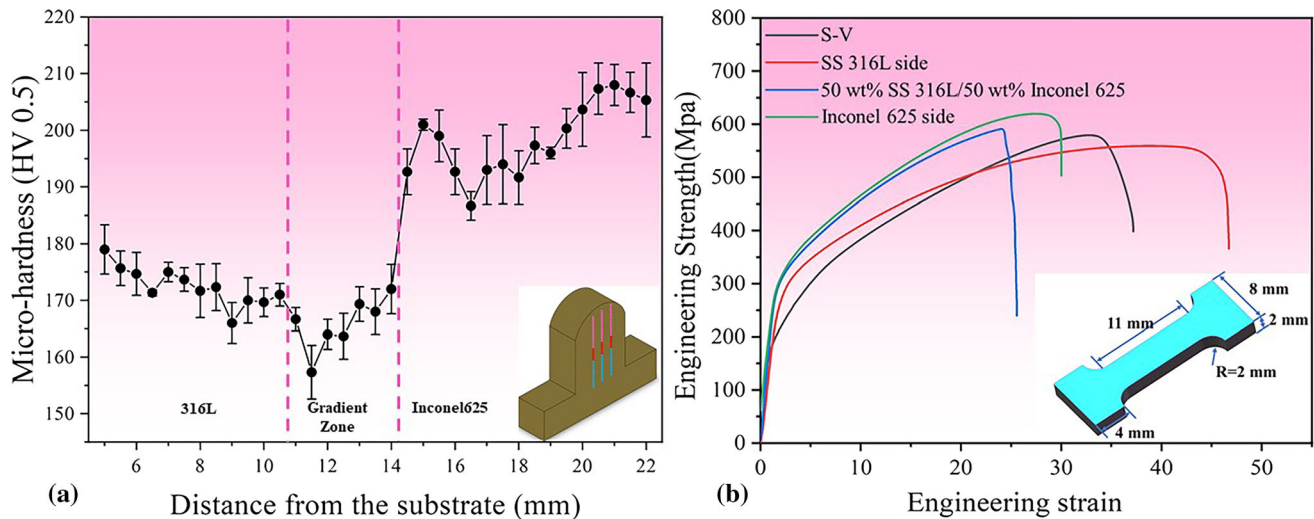**Fig. 6** The composition distribution of SS 316L-Inconel 625 FGM

Fig. 7 (a) Microhardness distribution along the deposition direction and (b) The tensile strain-strength curve

and the inherent characteristics of γ-austenite is soft (Ref 45). At the same time, the enhancement elements such as Nb and Mo are segregated in the first layer of 50 wt.% SS 316L/50 wt.% Inconel 625 transition zone, and the content is also small. As a result, the microhardness value drops to a minimum (157 HV) (Ref 21), a similar situation was also found in the research of Shah et al. (Ref 11). Then, with the addition of Inconel 625, the content of Ni, Cr and Mo elements increase, the solid solution strengthening effect of austenite is enhanced, and the microhardness increases (Ref 44). In addition, the concentration of Nb element in the inter-dendritic region also play a crucial role in the increase in microhardness, therefore, the microhardness increases with the increase of Inconel 625 (Ref 11, 44). At the top of Inconel 625 region, the columnar structure is transformed into equiaxed structure, and the microhardness value shows an upward trend, and the microhardness value reaches the maximum (208 HV).

3.4 Tensile Test

Figure 7(b) shows the tensile strain-strength curves, and the tensile test results are presented in Table 3. The tensile results of the tensile specimens in the vertical direction: the ultimate tensile strength, yield strength and elongation are 554.12 ± 7.44 340.79 ± 4.13 and 26.65 ± 0.27%, respectively. The tensile results are equivalent to the tensile properties of SS 316L-Inconel 625 FGM manufactured with LMD technology and higher than the typical properties of SS 316L

obtained by forging (Ref 55). The tensile results of tensile specimens with different composition regions in the horizontal direction are also presented in Table 3. The tensile results show that the ultimate tensile strength and yield strength of the SS 316L-Inconel 625 FGM increase gradually with the increase in Inconel 625 when the composition gradient is 50%. The 100 wt.% SS 316L region has the highest elongation (40.23 ± 2.58%), and the 50% SS 316L/50% Inconel 625 and 100 wt.% Inconel 625 regions are 26 ± 0.98% and 28.23 ± 1.24%, respectively. The fracture morphology and element distribution in the vertical direction are shown in Fig. 8, and the EDS analysis results of the fracture morphology show that Fe and Ni element are 52 and 25% respectively. Therefore, the fracture position is between 100 and 50 wt.% SS 316L/50 wt.% Inconel 625. The horizontal tensile test results show that the tensile properties of 316L-Inconel 625 FGM increase with the increase in Inconel 625, when the composition gradient is 50%. However, there are some errors between the actual and design element distribution due to the high heat input and complex thermal cycle. As a result, a composition region with a Inconel 625 concentration of 20 ~ 30% is existed. Previous studies have shown that the mechanical

Table 3 Tensile results of specimens

Tensile direction	Samples	Ultimate tensile strength, MPa	Yield strength, MPa	Elongation, %
Vertical	S-V	554.1 ± 7.4	340.8 ± 4.1	26.7 ± 0.3
	100 wt.% SS 316L	566.8 ± 12.1	295.8 ± 1.0	40.2 ± 2.6
Horizontal	50 wt.% SS 316L	617.1 ± 8.9	390.0 ± 7.2	26.0 ± 1.0
	100 wt.% Inconel 625	708.0 ± 7.2	402.7 ± 1.1	28.2 ± 1.2
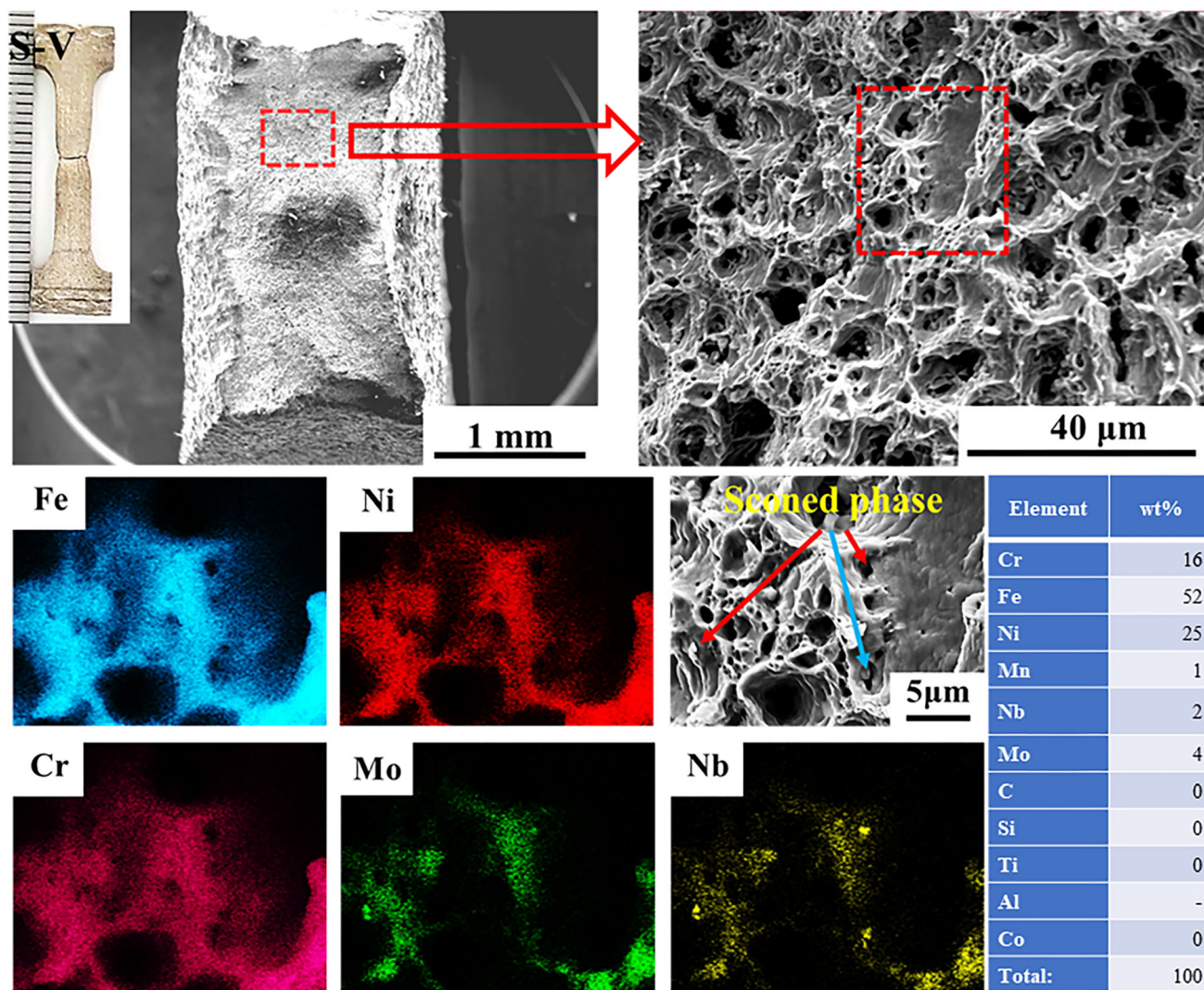
Fig. 8 Fracture morphology and element distribution of tensile specimens in the vertical direction

properties of FGM deteriorate within this composition range (Ref 21, 40).

Previous works have shown that the grain growth direction of SS 316L-Inconel 625 FGM parts is dominated by the deposition direction. Therefore, the microstructure perpendicular to the deposition direction is mostly cellular structure (Ref 50, 56). The yield strength is inversely proportional to the size of cellular structure, and the size of cellular structure increases gradually with the increase in deposition height (Ref 21). When the content of Inconel 625 is low ($<$ 50 wt.% Inconel 625), ferrite disappears (Ref 21), enhancing elements such as Mo and Nb segregate to the formation of Laves, and the heat accumulation resulted in the size of cellular structure increases (Ref 21, 40). Therefore, the fracture position of the tensile specimen in the vertical direction is between 100 and 50 wt.% SS 316L. The fracture mode of test specimen is ductile fracture, and the fracture surface is fibrous, indicating that sufficient deformation occurred before fracture. The fracture morphology is deep dimple and sharp crack edge, and a small amount of second phase is distributed in the depression, which has the characteristics of micropore aggregation and ductile fracture. The distribution of composition shows that Fe, Ni and Cr elements are uniformly distributed at the fracture, and Mo and Nb elements are segregated. The small particles in the dimples are rich in Mo and Nb elements, which is related to the existence of Laves phase.

4. Conclusion

In the present research, thin-walled structure of SS 316L-Inconel 625 FGM was designed by dual-wire plasma arc welding. The deposition process was achieved by changed the wire feeding speed of SS 316L and Inconel 625 welding wire. According to phase evolution, microstructure, composition distribution and mechanical properties in the building direction were examined, and the following conclusions were drawn:

(1) A FGM with a composition gradient of 50 wt.% from SS 316L to Inconel 625 was successfully manufactured by dual-wire plasma arc welding. The microstructure was dominated by columnar and equiaxed dendritic structures, and the primary dendrite arm spacing increased significantly along the building direction. The microstructure gradually changed from FCC + BCC to FCC phase. EBSD detection showed that the grain growth was mainly $<$ 001 $>$ orientation.

(2) The element distribution showed that the actual composition gradient had three composition gradients in the transition zone due to the influence of remelting, which was large than the design composition gradient. The results of EDS detection of the second phase particles in transition zone and 100 wt.% Inconel 625 indicated the existence of the laves phase.

(3) The microhardness of the 100 wt.% SS 316L region gradually decreased firstly along the building direction, and reached a minimum (157 HV) between the 100 and 50 wt.% SS 316L region. Subsequently, with the continuous increase in Inconel 625, the microhardness also gradually increased, and with a maximum microhardness of 208 HV at the top of 100 wt.% Inconel 625.

(4) The ultimate tensile strength, yield strength and elongation of the vertical tensile specimen were 554.12 ± 7.44, 340.79 ± 4.13 and $26.65 \pm 0.27\%$, respectively, and the tensile fracture mechanism was typical ductile fracture.

References

1. J.P. Oliveira, A. Shamsolhodaei, J. Shen, J.G. Lopes, R.M. Gonçalves, M. de Brito Ferraz, L. Piçarra, Z. Zeng, N. Schell, N. Zhou and, H. Seop Kim, Improving the Ductility in Laser Welded Joints of CoCrFeMnNi High Entropy Alloy to 316 Sainless Steel, *Mater. Des.*, 2022 https://doi.org/10.1016/j.matdes.2022.110717

2. A.M.S. Costa, J.P. Oliveira, V.F. Pereira, C.A. Nunes, A.J. Ramirez and, A.P. Tschiptschin, Ni-Based Mar-M247 Superalloy as a Friction Stir Processing Tool, *J. Mater. Process Tech.*, 2018, **262**, p 605–614. https://doi.org/10.1016/j.jmatprotec.2018.07.034

3. L. Yan, Y.T. Chen and, F. Liou, Additive Manufacturing of Functionally Graded Metallic Materials Using Laser Metal Deposition, *Addit Manuf*, 2020, **31**, p 100901. https://doi.org/10.1016/j.addma.2019.100901

4. J. Coleman, A. Plotkowski, B. Stump, N. Raghavan, A.S. Sabau, M.J.M. Krane, J. Heigel, R.E. Ricker, L. Levine and, S.S. Babu, Sensitivity of Thermal Predictions to Uncertain Surface Tension Data in Laser Additive Manufacturing, *J. Heat Trans.*, 2020 https://doi.org/10.1115/1.4047916

5. G. Xu, R. Wu, K. Luo and, J. Lu, Effects of Heat Treatment on Hot Corrosion Behavior of Directed Energy Deposited In718/316L Functionally Graded Material, *Corros. Sci.*, 2022, **197**, p 110068

6. U. Savitha, G. Jagan Reddy, A. Venkataramana, A. Sambasiva Rao, A.A. Gokhale and, M. Sundararaman, Chemical Analysis, Structure and Mechanical Properties of Discrete and Compositionally Graded SS316–IN625 Dual Materials, *Mater. Sci. Eng.: A*, 2015, **647**, p 344–352. https://doi.org/10.1016/j.msea.2015.09.001

7. R. Ghanavati and H. Naffakh-Moosavy, Additive Manufacturing of Functionally Graded Metallic Materials: A Review of Experimental and Numerical Studies, *J. Mater. Res. Technol.*, 2021, **13**, p 1628–1664. https://doi.org/10.1016/j.jmrt.2021.05.022

8. A. Strojny-Nedza, K. Pietrzak and, W. Weglewski, The Influence of Al2O3 Powder Morphology on the Properties of Cu-Al2O3 Composites Designed for Functionally Graded Materials (FGM), *J. Mater. Eng. Perform.*, 2016, **25**(8), p 3173–3184. https://doi.org/10.1007/s11665-016-2204-3

9. M. K, FGM Activities in Japan, *Compos. Part B: Eng.*, 1997, **28**(1–2), p 1–4. https://doi.org/10.1016/S1359-8368(96)00016-9

10. B.E. Carroll, R.A. Otis, J.P. Borgonia, J.O. Suh, R.P. Dillon, A.A. Shapiro, D.C. Hofmann, Z.K. Liu and, A.M. Beese, Functionally Graded Material of 304L Stainless Steel and inconel 625 Fabricated by Directed Energy Deposition: Characterization and Thermodynamic Modeling, *Acta Mater.*, 2016, **108**, p 46–54. https://doi.org/10.1016/j.actamat.2016.02.019

11. K. Shah, I. ulHaq, A. Khan, S.A. Shah, M. Khan and, A.J. Pinkerton, Parametric Study of Development of Inconel-Steel Functionally Graded Materials by Laser Direct Metal Deposition, *Mater. Des.*, 2014, **54**, p 531–538. https://doi.org/10.1016/j.matdes.2013.08.079

12. S. Mohan Kumar, A. Rajesh Kannan, N. Pravin Kumar, R. Pramod, N. Siva Shanmugam, A.S. Vishnu and, S.G. Channabasavanna, Microstructural Features and Mechanical Integrity of Wire Arc Additive Manufactured SS321/Inconel 625 Functionally Gradient

Material, *J. Mater. Eng. Perform.*, 2021, **30**(8), p 5692–5703. https://doi.org/10.1007/s11665-021-05617-3

13. G.H. Loh, E.J. Pei, D. Harrison and, M.D. Monzon, An Overview of Functionally Graded Additive Manufacturing, *Addit Manuf*, 2018, **23**, p 34–44. https://doi.org/10.1016/j.addma.2018.06.023

14. D. Raabe, C.C. Tasan and, E.A. Olivetti, Strategies for Improving the Sustainability of Structural Metals, *Nature*, 2019, **575**, p 64–74

15. W. Zixian, G. Shi, Y. Yang, X. Wen, C. Guo, and A. Zhang, Micro Metal Additive Manufactured Low-Loss Slotted Rectangular Waveguides Operating at 220-500 GHz, *Front. Phys.*, 2021 https://doi.org/10.3389/fphy.2021.696318

16. A. Singh, S. Kapil, and M. Das, A Comprehensive Review of the Methods and Mechanisms for Powder Feedstock Handling in Directed Energy Deposition, *Addit Manuf*, 2020, **35**, p 101388. https://doi.org/10.1016/j.addma.2020.101388

17. W. Meng, W.H. Zhang, W. Zhang, X.H. Yin, and B. Cui, Fabrication of Steel-Inconel Functionally Graded Materials by Laser Melting Deposition Integrating with Laser Synchronous Preheating, *Opt. Laser Technol.*, 2020, **131**, p 106451. https://doi.org/10.1016/j.optlastec.2020.106451

18. A.U. Rehman, N.K. Babu, M.K. Talari, Y.S. Usmani, and H. Al-Khalefah, Microstructure and Mechanical Property Correlation Between Rotary Friction Welded Nitinol–Nitinol Joints, *Front. Mater.*, 2021 https://doi.org/10.3389/fmats.2021.726383

19. A. Reichardt, R.P. Dillon, J.P. Borgonia, A.A. Shapiro, B.W. McEnerney, T. Momose, and P. Hosemann, Development and Characterization of Ti-6Al-4V to 304L Stainless Steel Gradient Components Fabricated with Laser Deposition Additive Manufacturing, *Mater. Des.*, 2016, **104**, p 404–413. https://doi.org/10.1016/j.matdes.2016.05.016

20. C. Wei, Z. Sun, Q. Chen, Z. Liu, and L. Li, Additive Manufacturing of Horizontal and 3D Functionally Graded 316L/Cu10Sn Components via Multiple Material Selective Laser Melting, *J. Manuf. Sci. Eng.*, 2019 https://doi.org/10.1115/1.4043983

21. Y. Su, B. Chen, C. Tan, X. Song, and J. Feng, Influence of Composition Gradient Variation on the Microstructure and Mechanical Properties of 316 L/Inconel718 Functionally Graded Material Fabricated by Laser Additive Manufacturing, *J. Mater. Process Tech.*, 2020, **283**, p 116702. https://doi.org/10.1016/j.jmatprotec.2020.116702

22. E. Tenuta, A. Nycz, M. Noakes, S. Simunovic, and M.H.A. Piro, Material Properties and Mechanical Behaviour of Functionally Graded Steel Produced by Wire-Arc Additive Manufacturing, *Addit. Manuf.*, 2021, **46**, p 102175. https://doi.org/10.1016/j.addma.2021.102175

23. W.C. Ke, J.P. Oliveira, B.Q. Cong, S.S. Ao, Z.W. Qi, B. Peng, and Z. Zeng, Multi-Layer Deposition Mechanism in Ultra High-Frequency Pulsed Wire Arc Additive Manufacturing (WAAM) of NiTi Shape Memory Alloys, *Addit. Manuf.*, 2022, **50**, p 102513. https://doi.org/10.1016/j.addma.2021.102513

24. A. Ramalho, T.G. Santos, B. Bevans, Z. Smoqi, J.P. Oliveira, and P. Rao, Effect of Contaminations on the Acoustic Emissions During Wire and Arc Additive Manufacturing of 316L Stainless Steel, *Addit. Manuf.*, 2022, **51**, p 102585. https://doi.org/10.1016/j.addma.2021.102585

25. Q.K. Shen, X.D. Kong, X.Z. Chen, X.K. Yao, V.B. Deev, and E.S. Prusov, Powder Plasma Arc Additive Manufactured CoCrFeNi(SiC)(x) High-Entropy Alloys: Microstructure and Mechanical Properties, *Mater. Lett.*, 2021 https://doi.org/10.1016/j.matlet.2020.128736

26. S. Qingkai, and K.C.Y.D.P. XiangdongXizhangXukaiVBES, Powder Plasma Arc Additive Manufactured CoCrFeNi(SiC)x High-Entropy Alloys: Microstructure and Mechanical Properties, *Mater. Lett.*, 2021, **282**, p 128736. https://doi.org/10.1016/j.matlet.2020.128736

27. X. Chen, J. Han, J. Wang, Y. Cai, G. Zhang, L. Lianzhong, Y. Xin, and Y. Tian, A Functionally Graded Material from TC4 to 316L Stainless Steel Fabricated by Double-Wire + Arc Additive Manufacturing, *Mater. Lett.*, 2021, **300**, p 130141. https://doi.org/10.1016/j.matlet.2021.130141

28. G. Marinelli, F. Martina, H. Lewtas, D. Hancock, S. Ganguly, and S. Williams, Functionally Graded Structures of Refractory Metals by Wire Arc Additive Manufacturing, *Sci. Technol. Weld. Jol.*, 2019, **24**(5), p 495–503. https://doi.org/10.1080/13621718.2019.1586162

29. C. Shen, Z. Pan, D. Cuiuri, J. Roberts, and H. Li, Fabrication of Fe-FeAl Functionally Graded Material Using the Wire-Arc Additive Manufacturing Process, *Metall. Mater. Trans. B*, 2015, **47**(1), p 763–772. https://doi.org/10.1007/s11663-015-0509-5

30. J. Han, L. Lianzhong, Y. Xin, X. Chen, G. Zhang, Y. Cai, and Y. Tian, Microstructure and Mechanical Properties of a Novel Functionally Graded Material from Ti6Al4V to Inconel 625 Fabricated by Dual Wire + Arc Additive Manufacturing, *J. Alloy. Compd.*, 2022, **903**, p 163981. https://doi.org/10.1016/j.jallcom.2022.163981

31. T.A. Rodrigues, N. Bairrão, F.W.C. Farias, A. Shamsolhodaei, J. Shen, N. Zhou, E. Maawad, N. Schell, T.G. Santos, and J.P. Oliveira, Steel-Copper Functionally Graded Material Produced by Twin-Wire and Arc Additive Manufacturing (T-WAAM), *Mater. Des.*, 2022, **213**, p 110270. https://doi.org/10.1016/j.matdes.2021.110270

32. C. Shen, K.-D. Liss, M. Reid, Z. Pan, X. Hua, F. Li, G. Mou, Y. Huang, B. Dong, D. Luo, and H. Li, Effect of the Post-Production Heat Treatment on Phase Evolution in the fe3Ni–FeNi Functionally Graded Material: An in-Situ Neutron Diffraction Study, *Intermetallics*, 2021, **129**, p 107032. https://doi.org/10.1016/j.intermet.2020.107032

33. T.S. Senthil, S.R. Babu, M. Puviyarasan, and V. Dhinakaran, Mechanical and Microstructural Characterization of Functionally Graded INCONEL 825-SS316L Fabricated Using Wire Arc Additive Manufacturing, *J. Mater. Res. Technol.*, 2021, **15**, p 661–669. https://doi.org/10.1016/j.jmrt.2021.08.060

34. J.R. Zhang, X.J. Di, X. Jiang, and C.N. Li, Effect of Synchronous Electromagnetic Stirring on Laves Phase Morphology and Mechanical Property of Inconel625-HSLA Steel Functionally Graded Material Fabricated by Wire Arc Additive Manufacturing, *Mater. Lett.*, 2022, **316**, p 132015. https://doi.org/10.1016/j.matlet.2022.132015

35. D. Zaguliaev, S. Konovalov, Y. Ivanov, and V. Gromov, Effect of Electron-Plasma Alloying on Structure and Mechanical Properties of Al-Si Alloy, *Appl. Surf. Sci.*, 2019, **498**, p 143767. https://doi.org/10.1016/j.apsusc.2019.143767

36. V. Hutsaylyuk, M. Student, V. Posuvailo, O. Student, V. Hvozdets'kyi, P. Maruschak, and V. Zakiev, The role of Hydrogen in the Formation of Oxide-Ceramic Layers on Aluminum Alloys During their Plasma-Electrolytic Oxidation, *J. Market. Res.*, 2021, **14**, p 1682–1696. https://doi.org/10.1016/j.jmrt.2021.07.082

37. W. Yangfan, C. Xizhang, and S. Chuanchu, Microstructure and Mechanical Properties of INCONEL 625 Fabricated by Wire-Arc Additive Manufacturing, *Surf. Coat. Technol.*, 2019, **374**, p 116–123. https://doi.org/10.1016/j.surfcoat.2019.05.079

38. T. Pinomaa, M. Lindroos, M. Walbruhl, N. Provatas, and A. Laukkanen, The Significance of Spatial Length Scales and Solute Segregation in Strengthening Rapid Solidification Microstructures of 316L Stainless Steel, *Acta Mater.*, 2020, **184**, p 1–16. https://doi.org/10.1016/j.actamat.2019.10.044

39. G.T. Gray, V. Livescu, P.A. Rigg, C.P. Trujillo, C.M. Cady, S.R. Chen, J.S. Carpenter, T.J. Lienert, and S.J. Fensin, Structure/Property (Constitutive and Spallation Response) of Additively Manufactured 316L Stainless Steel, *Acta Mater.*, 2017, **138**, p 140–149. https://doi.org/10.1016/j.actamat.2017.07.045

40. S.H. Kim, H. Lee, S.M. Yeon, C. Aranas, K. Choi, J. Yoon, S.W. Yang, and H. Lee, SELECTIVE Compositional Range Exclusion via Directed Energy Deposition to Produce a Defect-free INCONEL 718/SS 316L Functionally Graded Material, *Addit. Manuf.*, 2021, **47**, p 102288. https://doi.org/10.1016/j.addma.2021.102288

41. W. Li, X. Chen, L. Yan, J. Zhang, X. Zhang, and F. Liou, Additive Manufacturing of a New Fe-Cr-Ni Alloy with Gradually Changing Compositions with Elemental Powder Mixes and Thermodynamic Calculation, *Int. J. Adv. Manuf. Tech.*, 2017, **95**(1–4), p 1013–1023. https://doi.org/10.1007/s00170-017-1302-1

42. D.Y. Deng, R.L. Peng, H. Brodin, and J. Moverare, Microstructure and Mechanical Properties of Inconel 718 Produced by Selective Laser Melting: Sample Orientation Dependence and Effects of Post Heat Treatments, *Mat. Sci. Eng. A-Struct.*, 2018, **713**, p 294–306. https://doi.org/10.1016/j.msea.2017.12.043

43. D.C. Kong, C.F. Dong, S.L. Wei, X.Q. Ni, L. Zhang, R.X. Li, L. Wang, C. Man and X.G. Li, About Metastable Cellular Structure in Additively Manufactured Austenitic Stainless Steels, *Addit. Manuf.*, 2021, **38**, p 101804. https://doi.org/10.1016/j.addma.2020.101804

44. D. Wu, X. Liang, Q. Li, and L. Jiang, Laser Rapid Manufacturing of Stainless Steel 316L/Inconel718 Functionally Graded Materials: Microstructure Evolution and Mechanical Properties, *Int. J. Opt.*, 2010, **2010**, p 1–5. https://doi.org/10.1155/2010/802385

45. Y. Zhong, Z.Z. Zheng, J.J. Li, and C. Wang, Fabrication of 316L Nuclear Nozzles on the Main Pipeline with Large Curvature by CMT Wire Arc Additive Manufacturing and Self-Developed Slicing Algo-

rithm, *Mat. Sci. Eng. A-Struct.*, 2021, **820**, p 141539. https://doi.org/10.1016/j.msea.2021.141539

46. W. Li, L. Yan, X. Chen, J. Zhang, X. Zhang, and F. Liou, Directed Energy Depositing a New Fe-Cr-Ni alloy with gradually changing Composition with Elemental Powder Mixes and PARTICLE size' Effect in Fabrication Process, *J. Mater. Process Tech.*, 2018, **255**, p 96–104. https://doi.org/10.1016/j.jmatprotec.2017.12.010

47. B.R. Barbero, and E.S. Ureta, Comparative study of Different Digitization Techniques and their Accuracy, *Comput. Aided Design*, 2011, **43**(2), p 188–206. https://doi.org/10.1016/j.cad.2010.11.005

48. R. Ghanavati, H. Naffakh-Moosavy, and M. Moradi, Additive Manufacturing of thin-Walled SS316L-IN718 Functionally Graded Materials by Direct Laser Metal Deposition, *J. Mater. Res. Technol.*, 2021, **15**, p 2673–2685. https://doi.org/10.1016/j.jmrt.2021.09.061

49. D. Verdi, M.A. Garrido, C.J. Munez, and P. Poza, Microscale Effect of High-Temperature Exposition on Laser Cladded Inconel 625-Cr3C2 Metal Matrix Composite, *J. Alloys Compd.*, 2017, **695**, p 2696–2705. https://doi.org/10.1016/j.jallcom.2016.11.185

50. Y.M. Wang, T. Voisin, J.T. McKeown, J. Ye, N.P. Calta, Z. Li, Z. Zeng, Y. Zhang, W. Chen, T.T. Roehling, R.T. Ott, M.K. Santala, P.J. Depond, M.J. Matthews, A.V. Hamza, and T. Zhu, Additively Manufactured Hierarchical Stainless Steels with High Strength and Ductility, *Nat. Mater.*, 2018, **17**(1), p 63–71. https://doi.org/10.1038/nmat5021

51. H. Xiao, S.M. Li, X. Han, J. Mazumder, and L.J. Song, Laves Phase Control of Inconel 718 Alloy using Quasi-Continuous-Wave Laser Additive Manufacturing, *Mater. Des.*, 2017, **122**, p 330–339. https://doi.org/10.1016/j.matdes.2017.03.004

52. B. Chen, Y. Su, Z.H. Xie, C.W. Tan, and J.C. Feng, Development and Characterization of 316L/Inconel625 Functionally Graded Material Fabricated by Laser Direct Metal Deposition, *Opt. Laser Technol.*, 2020, **123**, p 105916. https://doi.org/10.1016/j.optlastec.2019.105916

53. E. Chauvet, P. Kontis, E.A. Jagle, B. Gault, D. Raabe, C. Tassin, J.J. Blandin, R. Dendievel, B. Vayre, S. Abed, and G. Martin, Hot Cracking Mechanism Affecting a Non-Weldable Ni-Based superalloy Produced by Selective Electron BEAM Melting, *Acta Mater.*, 2018, **142**, p 82–94. https://doi.org/10.1016/j.actamat.2017.09.047

54. X. Chen, J. Li, X. Cheng, B. He, H. Wang, and Z. Huang, Microstructure and Mechanical Properties of the Austenitic Stainless Steel 316L Fabricated by Gas Metal Arc Additive Manufacturing, *Mater. Sci. Eng. A*, 2017, **703**, p 567–577. https://doi.org/10.1016/j.msea.2017.05.024

55. D.R. Feenstra, A. Molotnikov, and N. Birbilis, Effect of Energy Density on the Interface Evolution of Stainless Steel 316l Deposited Upon INC 625 via Directed Energy Deposition, *J. Mater. Sci.*, 2020, **55**(27), p 13314–13328. https://doi.org/10.1007/s10853-020-04913-y

56. M.S. Pham, B. Dovgyy, P.A. Hooper, C.M. Gourlay, and A. Piglione, The Role of Side-Branching in Microstructure Development in Laser Powder-Bed Fusion, *Nat. Commun.*, 2020, **11**(1), p 749. https://doi.org/10.1038/s41467-020-14453-3